

## THE X3 FLARE OF 2002 JULY 15

JING LI AND D. L. MICKEY

Institute for Astronomy, University of Hawaii, 2680 Woodlawn Drive, Honolulu, HI 96822;  
jing@ifh.hawaii.edu, mickey@ifh.hawaii.edu

AND

B. J. LABONTE

Johns Hopkins University, Applied Physics Laboratory, 11100 Johns Hopkins Road, Laurel, MD 20723-6099;  
barry.labonte@jhuapl.edu

Received 2004 June 14; accepted 2004 November 3

### ABSTRACT

An X3-class flare occurred on 2002 July 15 with white-light emission and a complex filament eruption. Observations were made in the optical continuum,  $H\alpha$ , UV continuum, microwave, and soft X-rays, as well as with high-cadence longitudinal magnetograms. Within the preflare phase, intense heating is observed accompanying upward motion of the filament. At the onset of the impulsive phase, filament Doppler acceleration is increased from  $-1.5$  to  $-7.0$  km s $^{-2}$ . Flare impulsive emission is double-peaked, possibly corresponding to two magnetic reconnection events: the first occurs above the active region in the corona, while the second takes place in a thin current sheet underneath the eruptive filament. It is probable that a twisted helical flux rope, seen in  $C\text{ IV }TRACE$  images, is formed during the second reconnection. The energy released by the white-light flare is  $\sim 10^{33}$  ergs and dominates the flare emission spectra. Within the flare impulsive phase, the emission profiles show both abrupt and gradual components in white light, UV, and  $H\alpha$ . These variations are independently reflected in the transverse motions of flare kernels: the abrupt emission phase corresponds to a rapid kernel motion, while the gradual phase corresponds to a more modest kernel motion.

*Subject headings:* Sun: coronal mass ejections (CMEs) — Sun: filaments — Sun: flares — Sun: magnetic fields

### 1. INTRODUCTION

On 2002 July 15 at 20:03 UT, an X3 flare occurred near the solar disk center ( $N18^\circ$ ,  $E00^\circ$ ) in NOAA Active Region 10030. The flare was detected at wavelengths from soft X-ray to microwave including the optical continuum and was accompanied by a complex filament eruption. At 20:26 UT, following the eruption of a parallel filament, a second flare occurred but with much lower energy release than the first flare. A flux rope halo coronal mass ejection (CME) was observed at  $2.0 R_\odot$  at 20:30 UT, followed by a second, larger CME at 21:06 UT. In the current work, we focus on the first flare at 20:03 UT.

The July 15 event has received considerable attention because it was well observed by many facilities. Liu et al. (2003) focused their discussion on flare morphologies made with  $TRACE$   $C\text{ IV}/UV$  emissions and longitudinal magnetograms taken by the Michelson Doppler Imager (MDI) on board *SOHO*. By examining time series magnetograms, they conclude that the magnetic field cancellation in the photosphere is the trigger of the flare. Gary & Moore (2004) offer a comparison between observations and models. Based on the time separation between microwave bursts and the appearance of the helical structure, they suggested that the initial instability supports the “magnetic breakout” model (Antiochos 1998; Antiochos et al. 1999), which indicates the flare initiation in the corona. The different conclusions reflect the complexity of the event and the difficulty in extracting definitive measurements that can be used to test models.

One of the most significant features of the July 15 flare is the optical continuum (white-light) enhancement. This was not studied by either Liu et al. (2003) or Gary & Moore (2004). Good white-light flare (WLF) observations are rare. According to the estimation made by Neidig & Cliver (1983), about  $15.5 \pm 4.5$  WLFs per year followed the maximum of solar cycle 21,

while only about 5–6 WLFs a year occurred during solar cycle 20 (McIntosh & Donnelly 1972). The WLF frequency trend with solar cycle suggests that the WLF visibility is increased as the observing technology is improved. Based on the trend, it is not surprising that WLFs have been most actively investigated by recent spacecraft observations (Sylwester & Sylwester 2000; Matthews et al. 2003; Metcalf et al. 2003). These studies confirmed a traditional claim regarding WLFs: they are associated with nonthermal processes producing hard X-ray emissions (e.g., Hudson 1972). On the other hand, the thermal components of the WLFs were detected during the late impulsive phase (Matthews et al. 2003). Considering the extreme density conditions in the optical flares and the unknown reason for their huge radiation loss (Neidig 1989), WLFs are important for understanding the flare energy release process. Our WLF observations have both high temporal and spatial resolution, which together provide insights when comparing with flare data at other wavelengths.

In this paper, we discuss comprehensive, time-resolved observations of the July 15 event taken over a wide range of wavelengths. Our goal is to examine the flare process independently of models, taking advantage of a wide range of high-quality, high time resolution observations. From these we propose a schematic magnetic model for the preflare and impulsive stages that illustrates several important aspects of the flare. We begin with a brief introduction of the instruments and data analysis used in this work in § 2. Observations on preflare and impulsive phenomena are presented in § 3. Discussions and schematic models are given in § 4. A summary is given in § 5.

### 2. DATA AND BASIC REDUCTIONS

Flare observations were made at Mees Solar Observatory (MSO), at the Owens Valley Solar Array (OVSA), and by the

TABLE 1  
CHARACTERISTICS OF INSTRUMENTS USED IN WLF OBSERVATIONS

Instrument	Band Center <sup>a</sup>	Bandpass <sup>b</sup>	$\Delta t$ <sup>c</sup> (s)	Pixel Size <sup>d</sup> (arcsec)
IVM.....	6300 Å	100 Å	1	$0.55 \times 0.55$
MCCD.....	6563 Å	18 Å	16	$2.45 \times 2.34$
TRACE.....	1600 Å	275 Å	2	$0.5 \times 0.5$
MDI/SOHO.....	6767.8 Å	0.094 Å	~120	$0.6 \times 0.6$
OVSA.....	1–18 GHz	200 MHz	4	...
GOES-8.....	1–8; 0.5–4 Å	...	3	...

<sup>a</sup> The central wavelength/frequency used in each instrument.

<sup>b</sup> The wavelength/frequency range covered by each instrument.

<sup>c</sup> The term  $\Delta t$  is the time cadence of the flare observations.

<sup>d</sup> The projected pixel size in arcseconds for each imaging instruments.

TRACE (Handy 1999) and SOHO spacecraft. Soft X-ray data are available from GOES-8. Table 1 summarizes the characteristics of the instruments used for our flare analysis. Unfortunately, RHESSI was in the night portion of its orbit at the time of the flare impulsive phase; therefore, we have no hard X-ray images.

### 2.1. Mees IVM

The Mees Imaging Vector Magnetograph (IVM; Mickey et al. 1996) observed the flare in the optical continuum. The IVM Data camera takes four Stokes images at 30 wavelength positions across the Fe I  $\lambda 6302.25$  line in about 2 minutes. Simultaneously, the IVM Geometry camera records the continuum through a 100 Å bandpass prefilter centered on the line. Each data file includes 120 images of mixed polarization states at an image cadence of 1 s.

We used the IVM Geometry data to construct images of the flare contrast, defined as  $\Delta I/I_0 = (I - I_0)/I_0$ , where  $I_0$  is the median image intensity made from nonflare frames. At most times the solar noise is 0.7% of the photospheric intensity per IVM pixel. The WLF sites are defined as the pixels where the contrast is greater than 5 times the noise. During moments of poor seeing, the image contrast near sunspots with large intensity gradients occasionally exceeds this threshold. Examining the total intensity, rather than the contrast, in the selected areas rejects these spurious features. A few WLF patches might be lost in this rejection if they were located on such a gradient and had a time history matched to the moments of worst seeing. However, given the location of the WLF on clean photosphere far from major spots, we think that this is not a significant problem. The largest observed WLF contrast was about 24%.

### 2.2. Mees MCCD

The Mees CCD (MCCD) imaging spectrograph (Penn et al. 1991) has a field of view  $4.8 \times 3.7$  and has a spectral range of 18 Å centered at H $\alpha$ . The spectrograph slit is oriented north-south, and the image is scanned east-west. Pixel scales are  $2''33$  spatially and 0.36 Å in the dispersion direction. Data with MCCD were taken continually from 16:20:59 to 21:13:35 UT on July 15 with temporal resolution of 16 s. The MCCD time is set by reference to a GPS signal, with a typical uncertainty that is less than 0.5 s.

### 2.3. TRACE 160 nm Channel

The flare in the transition region was observed by TRACE through the 160 nm UV filter. During the TRACE flare mode,

the exposure times vary from 0.02 to 0.4 s. We processed the raw images with the standard SolarSoft procedures (Freeland & Handy 1998). During the flare, the C IV lines dominate the 160 nm emission.

### 2.4. Owens Valley Solar Array

OVSA currently consists of two large 27 m antennas and three small 2 m antennas. Each is equipped with broadband logperiodic feeds capable of receiving 1–18 GHz. The receivers can tune to any harmonic of 200 MHz in the range 1–18 GHz and acquire phase lock in less than 20 ms. The system records left- and right-circular and linear polarized radiation.<sup>1</sup> In our analysis, the intensity in each frequency measured by Stokes  $I$  is used. The intensity enhancement occurred in all frequencies during the flare impulsive phase, but the strongest emissions were near 13 GHz (2.3 cm).

## 3. OBSERVATIONS

### 3.1. Region Evolution

Figure 1 shows NOAA AR 10030 (*top*), the longitudinal magnetogram (*middle*), and the H $\alpha$  image (*bottom*) on July 15. Rapid evolution of the magnetic field was concentrated in the eastern bipole, with both extension and shearing. However, the flare was mostly confined to the nearly static western part of the active region, within the rectangular area marked on the images. Sunspots in the flare vicinity are labeled P/N for positive/negative polarity. Two  $\delta$ -spots were formed by the groupings P3+ N2+N3 and P2+N1. The negative polarity plage between P1 and P2+P3, labeled X, is central to the flare. Two filaments border the plage; they are labeled in H $\alpha$  as F1 (western) and F2 (eastern) overlapping with magnetic neutral lines. Both filaments appear as reversed-S shaped sigmoids, implying negative magnetic helicity. The flare is connected with the eruption of F2.

Liu et al. (2003) suggested that changes in the photospheric magnetic field triggered the flare. Their conclusion was based on the magnetic flux measured as a function of time at one flare site. They found (1) magnetic cancellation on a timescale of hours and (2) a sudden dip in the magnetic flux coincident with the soft X-ray impulsive rise. This implies a close relationship between photospheric magnetic field sudden change and soft X-ray flare. We revisited their work but reached a different conclusion.

In Figure 2 we show the apparent magnetic flux as a function of time at two WLF sites, one of which, site 2, was near the  $p$  area described in Liu et al. (2003). We have overplotted the locations of the WLF patches at 20:04:59 UT against the MDI magnetogram in the figure. The time is when the apparent magnetic flux dips occurred and when the maximum WLFs were reached at the particular locations (see labels and contours on the image in Fig. 2). The fact that the magnetic flux dips are coincident in time with the white-light flare maxima is expected if these are artifacts caused by a change in the MDI line profile in response to the sudden photospheric emission enhancement. Moreover, as we discuss later, the flare impulsive phase was fully established by 20:03:30 UT. The sudden drop in the magnetic flux occurred around 20:05 UT, too late to be a trigger.

We do observe slow decrease in the magnetic fluxes at both sites in the July 15 data, consistent with those reported in Liu et al. (2003) (we obtain rates of change  $\sim 4.3 \times 10^{18}$  Mx hr<sup>-1</sup> for

<sup>1</sup> See <http://ovsa.ovro.caltech.edu/instrument.html>.

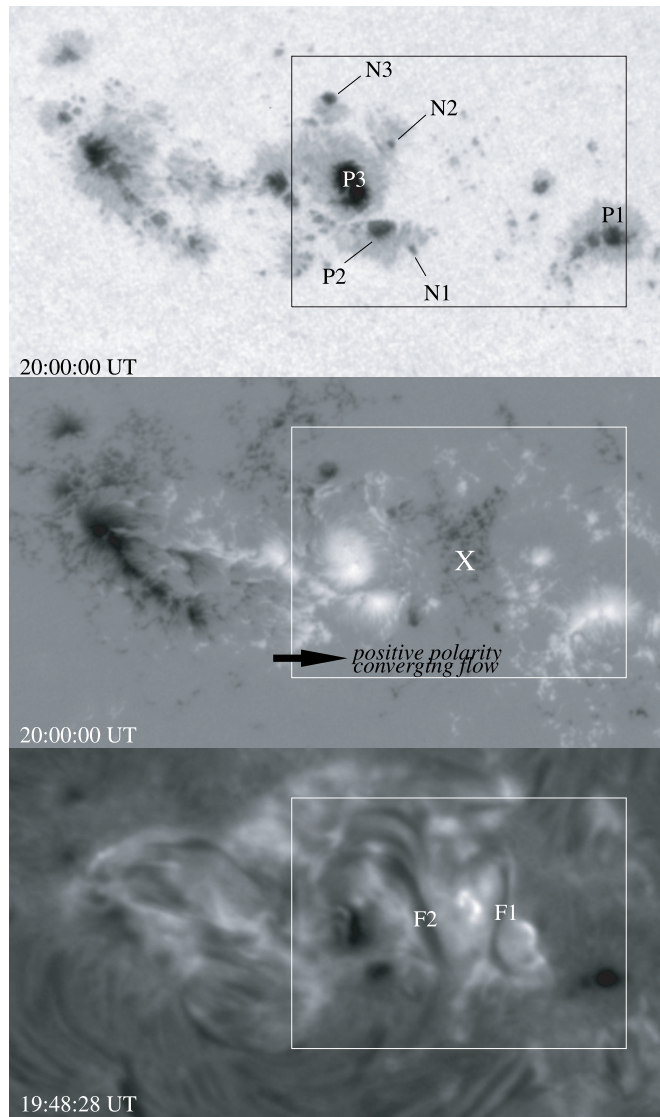


FIG. 1.—NOAA AR 10030 ( $N18^\circ, E00^\circ$ ). The flare was confined within the rectangular area. *Top*: MDI filtergram. Spot P2 along with N1, and spot P3 along with N2 and N3 formed two  $\delta$ -spots. *Middle*: MDI magnetogram. The region X is plage area. The black arrow indicates the converging flow direction by the positive polarity in the back of the active region. *Bottom*:  $H\alpha$  line-center image (courtesy BBSO). Two filaments adjacent to the X area are named F1 and F2. All images are  $300'' \times 180''$ . Rectangular area is  $150'' \times 121''$ .

site 1 and  $\sim -2.2 \times 10^{18} \text{ Mx hr}^{-1}$  for site 2). The fact that the WLF patch 1 contains only negative magnetic fluxes and that the patch 2 contains only positive magnetic fluxes indicates that the WLF patches overlap with footpoints of a magnetic loop. However, the observed slow changes cannot be viewed as the flare trigger, since the flux reduction rate appears steady and does not correlate with the flare onset. We conclude that the magnetic field data provide no evidence for a sudden change near the time of the flare and so provide no evidence regarding the triggering mechanism.

To investigate the flare initiative mechanism, we examine two significant motions in the photosphere near NOAA AR 10030 between July 11 and 17. Both motions are shown in Figure 3, as measured from *SOHO*/MDI intensity and magnetic images. First, the spot P3 showed counterclockwise (CCW) rotation about its center. We define  $\theta_3$  to be the position angle of the long axis of an ellipse fitted to the P3 spot isophotes (Fig. 3, *contour*). The

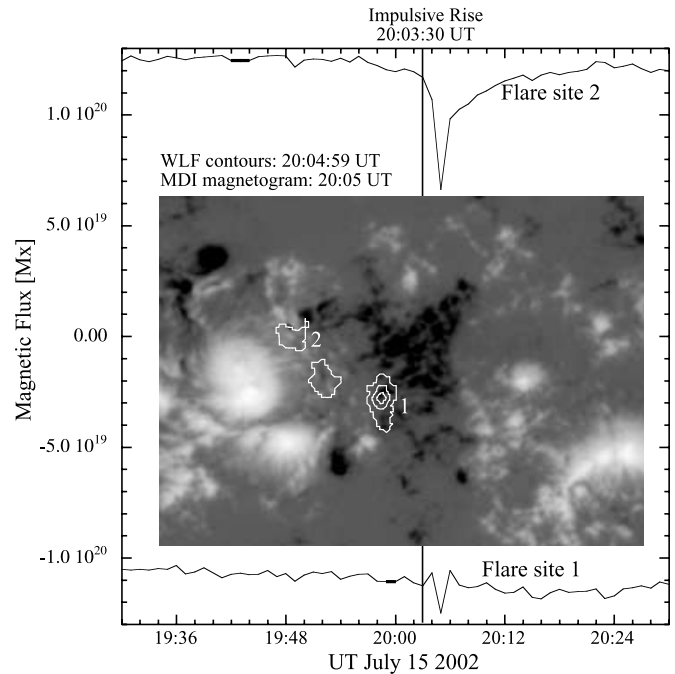


FIG. 2.—Total magnetic fluxes as a function of time. The image is an MDI magnetogram taken at 20:05 UT. Contours are WLF patches recorded at 20:04:59 UT. They represent the WL contrasts 0.05, 0.1, and 0.15. The magnetic fluxes are taken at two WLF sites numbered “1” and “2.” Site 1 contains only negative magnetic polarity. Likewise, site 2 contains only positive magnetic polarity. This indicates that WLF patches overlap with magnetic footpoints in the photosphere. It should be remembered that the flux’s sudden dips at both WLF sites are the result of the MDI spectral line distortion caused by the photospheric photometry enhancement, but not real magnetic field change.

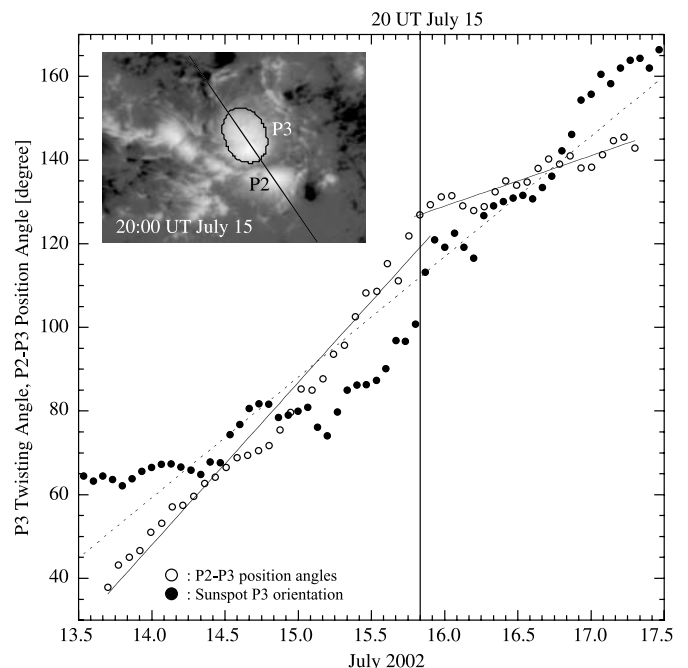


FIG. 3.—Position angle of the elongated P3 spot,  $\theta_3$ , and orientation of the P2-P3 axis,  $\theta_{2-3}$ , as functions of time. A sample ellipse used to measure  $\theta_3$  is illustrated in the panel, while the measured values are represented in the main figure by filled circles. The best-fit line has slope  $d\theta_3/dt = 29^\circ \pm 4^\circ \text{ day}^{-1}$  (dotted line). The  $\theta_{2-3}$  measurements are represented by circles and fitted in two time domains (solid lines). The P2-P3 orientation changed at rate  $d\theta_{2-3}/dt = 39^\circ \pm 3^\circ \text{ day}^{-1}$  before July 15, and  $d\theta_{2-3}/dt = 14^\circ \pm 1^\circ \text{ day}^{-1}$  after July 15.

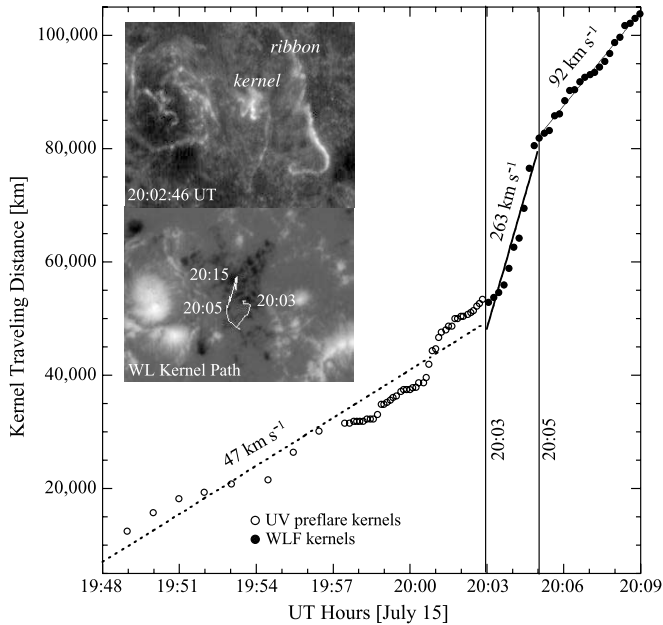


FIG. 4.—Preflare kernel and flare kernel transverse distance as function of time. The distances are the cumulative lengths of the kernel traveled from the first-appearing site. Preflare stage is between 19:48 and 20:03 UT, during which the transverse distances are measured with UV kernels from *TRACE* 1600 Å images (enclosed top image). They are fitted with a dotted line having slope  $47 \text{ km s}^{-1}$ . During the flare period, the distances are measured with WLF kernels from IVM images. They are fitted with a thick solid line having a slope  $263 \text{ km s}^{-1}$ , and a thin solid line having a slope  $92 \text{ km s}^{-1}$  corresponding to abrupt and gradual phases. The bottom image shows the WLF kernel path between 20:03 and 20:09 UT against a MDI magnetogram taken at 20:00 UT on July 15.

resulting average rotation rate was  $d\theta_3/dt = 29^\circ \pm 4^\circ \text{ day}^{-1}$ , which agrees well with the measurements of the same spot from *TRACE* continuum images (Brown et al. 2003). Spot rotation shows no significant variation at the time of the flare initiation. The second motion was the convergence of positive magnetic polarity to the eastern neutral line, which is indicated by a black arrow in the middle image of Figure 1. This can be viewed as relative motion of spot P2 passing by spot P3 from east to west. It is measured by  $\theta_{2-3}$ , which is the position angle of a straight line connecting the centers of the two spots measured counterclockwise from horizontal (see the line connecting the P2 and P3 centers in sub-image in Fig. 3). Measurements of  $\theta_{2-3}$  are more accurate than those of  $\theta_3$  because of short-term variations in the shape and intensity of the spot P3. We found that  $d\theta_{2-3}/dt$  was significantly different before and after the time of the flare (Fig. 3). Specifically, it decreased from  $d\theta_{2-3}/dt = 39^\circ \pm 3^\circ \text{ day}^{-1}$  before July 15 to  $d\theta_{2-3}/dt = 14^\circ \pm 1^\circ \text{ day}^{-1}$  after July 15. The converging flow was comparable to P3's rotation motion before the flare, but slowed down significantly after the flare. This indicates a kind of magnetic relaxation near the magnetic neutral line in the photosphere after the flare energy release. However, this motion cannot be viewed as the flare trigger because the flare initiated above F2, which is parallel to F1, but does not directly contact with the converging flow. We once again discuss the role of the convergence and investigate the flare trigger in § 4.

### 3.2. Preflare Activity

Before the flare, beginning at 19:46 UT, we observed the slow heating of a bright kernel in  $H\alpha$  and UV at X (see Fig. 1) and a ribbon on the western side of F1 (recall that the flare accompanies the eruption of F2). The kernel motion is recorded

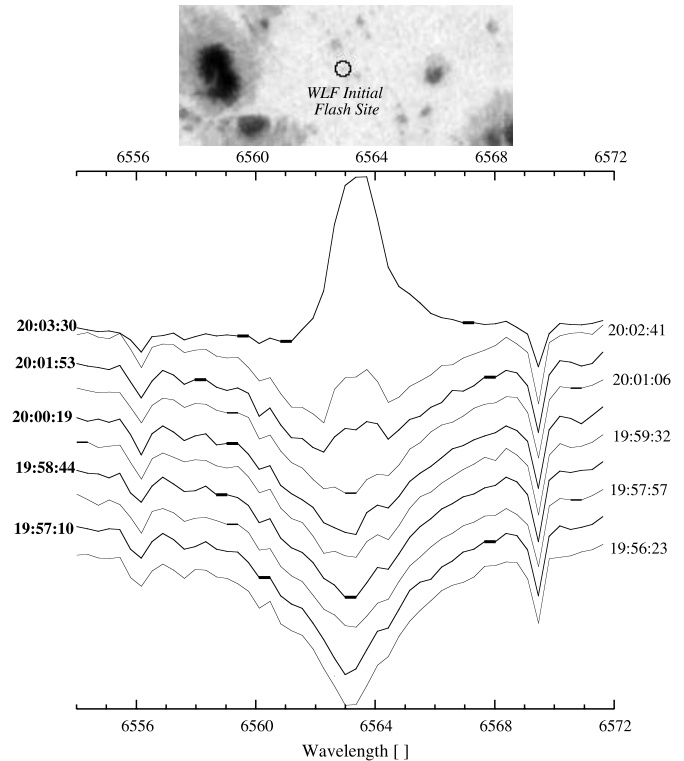


FIG. 5.—Series of  $H\alpha$  line profiles made at the location of the initial white-light flash site within a single M CCD pixel size,  $2''.45 \times 2''.34$ . The location is marked with a circle on the enclosed MDI filtergram image. A small pore is seen in the center of the circle. In the main plot, the x-axis is wavelength (Å) and the y-axis is the line intensity in DN. Times are UT.

between 19:48 and 20:03 UT in Figure 4. The average transverse speed is about  $47 \text{ km s}^{-1}$ .

As the heating increased between 19:58 and 20:03:30 UT,  $H\alpha$  red asymmetries appeared at the site of the initial WLF (Fig. 5). The magnitude of the red asymmetry indicates a constant downflow velocity  $\sim 45 \text{ km s}^{-1}$  at the onset of WLF, and this downflow was confined to a single M CCD pixel ( $2''.45 \times 2''.34$ ). At 20:03:30 UT,  $H\alpha$  first appeared in emission signaling the rise of the impulsive phase (Fig. 5). Red asymmetries are common at the onset of flares (e.g., Tang 1983; Ichimoto & Kurokawa 1984; Neidig et al. 1993). They are explained as the chromospheric compression caused by the explosive heating of the chromosphere (Abbett & Hawley 1999). Because we observe  $H\alpha$  red asymmetries prior to the impulsive rise, and overlapping with the initial WLF site, it appears that the preflare heating in this particular case became unusually intense.

Filament F2 began to lift at 20:01:22 UT (Fig. 6, large inset). The initial upward motion occurred in the southern part of the filament, which is outlined by a contour in  $H\alpha$  image in the figure. As can be seen in Figure 6, the upward acceleration of the southern part of the filament changed dramatically at 20:03 UT. The acceleration was  $-1.5 \text{ km s}^{-2}$  before and  $-7.0 \text{ km s}^{-2}$  after 20:03 UT. Evidently, the onset of the flare impulsive phase coincided with an increase in the net force on the filament. This disagrees with the observations made by Kahler et al. (1988), in which the filament accelerations started in preflare phase and were kept constant through impulsive phases, but agrees with an observation of a limb event made by Ohyama & Shibata (1997). In their observation, they recorded that the ejecta acceleration is coincident with the hard X-ray impulsive onset. We will discuss their observation further in § 4.

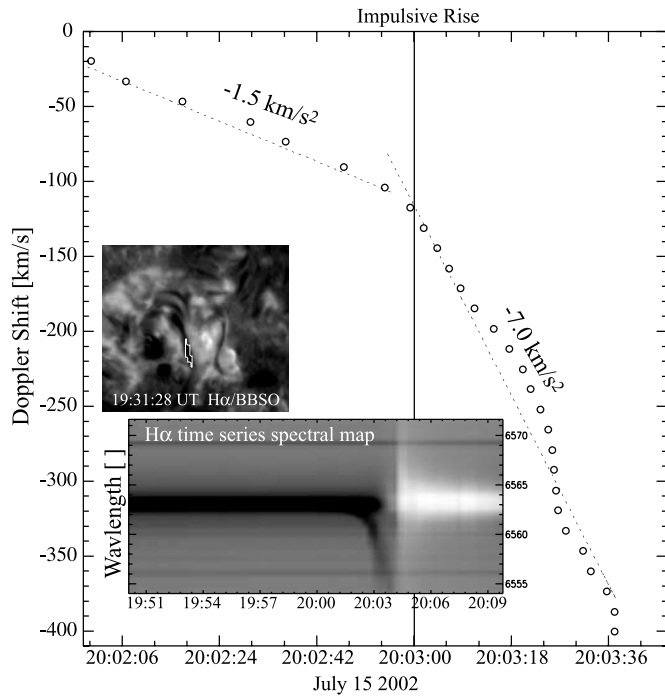


FIG. 6.—Doppler shifts as function of time on the part of the eastern filament (F2). The small inset shows an  $H\alpha$  line-center image (courtesy BBSO). The contour marks the region of F2 from which the Doppler shift was measured. The large inset is the time series  $H\alpha$  spectral map. It is made from the contoured area in the small panel. In the map, the bright features represent the  $H\alpha$  emission lines, and the dark features represent absorption. The derived line-of-sight acceleration shows a marked difference before and after 20:03 UT, the time of the flare.

### 3.3. Eruptive Phase

At 20:03:30 UT, the initial WLF occurred overlapping with a small pore, presumably representing a magnetic footpoint (Fig. 5, *enclosed image*). Meanwhile, the acceleration of filament F2 was observed in both cool  $H\alpha$  and hot  $C\text{ IV}$  lines.

The vertical acceleration plotted in Figure 6 continued until the line shift exceeded the  $-480\text{ km s}^{-1}$  range of the MCCD. Filament F2 began to tear off from its southern part as the white-light emission began at a different location. For comparison, Figure 7 gives a series of simultaneous images:  $H\alpha$  blue wing from MCCD (*left*),  $C\text{ IV}/UV$  from TRACE (*middle*), and WL contrast from IVM (*right*). The first row of images shows the start of the impulsive phase. Flare patches and ribbons are cospatial at all three wavelengths. As in the preflare heating phase and at the onset of the impulsive phase, the flare ribbons straddle F1, not F2 (see Fig. 1). From there, the southern part of F2, labeled “filament leg” in the 20:04:17  $H\alpha$  blue wing image, erupted. Between 20:04:01 and 20:04:17 UT, flare emission ribbons displaced from F1 to F2. The latter whips open, pivoting on its northern end, when the filament is lifted into a loop and the “filament front” is seen. The loop velocity in the plane of the sky was  $540\text{ km s}^{-1}$ , and the total velocity of the  $H\alpha$  material thus exceeded  $700\text{ km s}^{-1}$  between 20:03 and 20:06 UT.

$C\text{ IV}$  eruption is not cospatial with that of  $H\alpha$  but is adjacent, encompassing the southern end of F2. The initial eruption is seen as a slowly brightening, thin sheet of upflowing material. By 20:04:17 UT when F2 was lifted into a loop, flare ribbons including WLF appear straddling F2, and the ribbons straddling F1 rapidly fade. A helix-like structure appeared in the  $C\text{ IV}$  TRACE image and was visible for about 1 minute (see the “helix” in UV/TRACE images in Fig. 7). It moves in the direction of F2 eruption with an average transverse velocity,  $870\text{ km s}^{-1}$ . Its birthplace

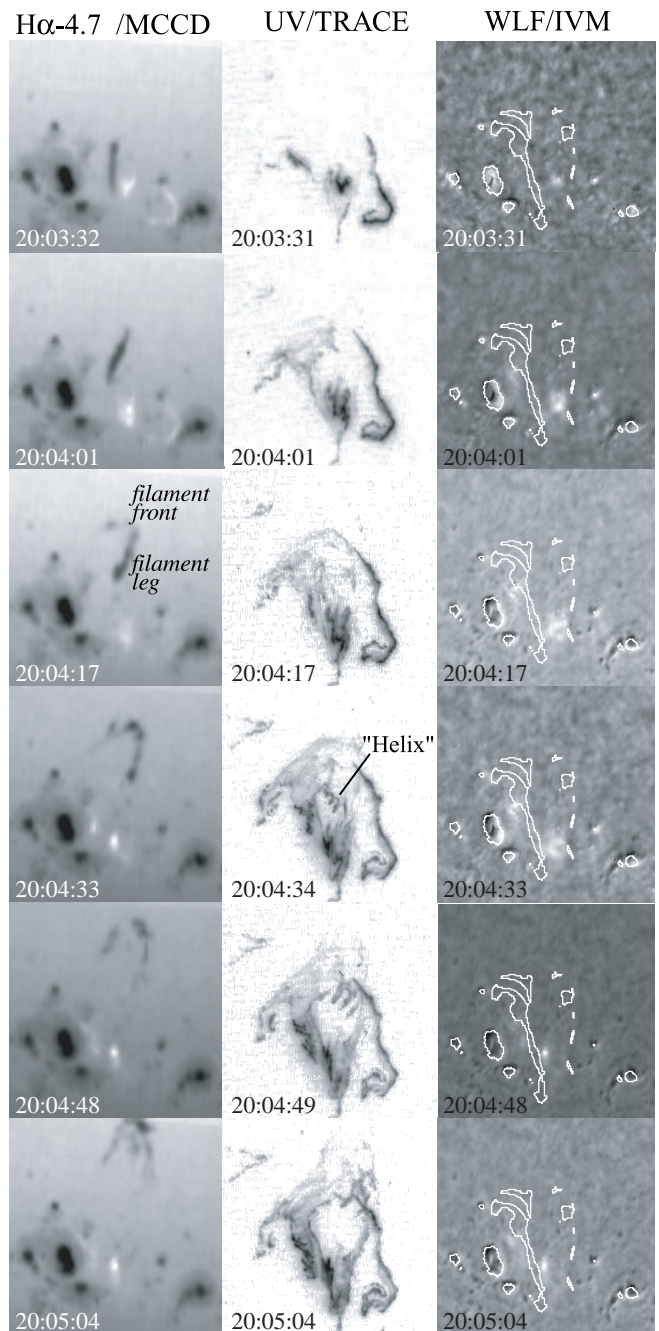


FIG. 7.—Simultaneous  $H\alpha$  blue wing (*left*), UV/TRACE (*middle*), and WLF/IVM contrast (*right*) images. The first row of images are taken at the impulsive rise 20:03:30 UT. The last row of images show the flares near the end of the abrupt phase. The WL images (*right column*) are contrast images that are made by subtracting a median image from individual images and dividing the median image. The contours represent the position of major sunspots and two filaments, F1 and F2. At  $H\alpha\ 4.7\ \text{\AA}$ , the  $H\alpha$  images represent a line-of-sight velocity  $-215\text{ km s}^{-1}$ . The size of all images is  $190'' \times 168''$ .

overlaps with the origin of  $H\alpha$  filament leg and flare ribbons, which implies a close correlation between the structure and filament eruption.

### 3.4. Flare Emissions in Time Sequence

Total flare time profiles in various wavelengths are shown in Figure 8, where the measurements have been converted to power units. The flare was an X3 flare measured in soft X-rays, with a peak flux recorded by the GOES detector of  $3.3 \times 10^{-4}\text{ W m}^{-2}$ .

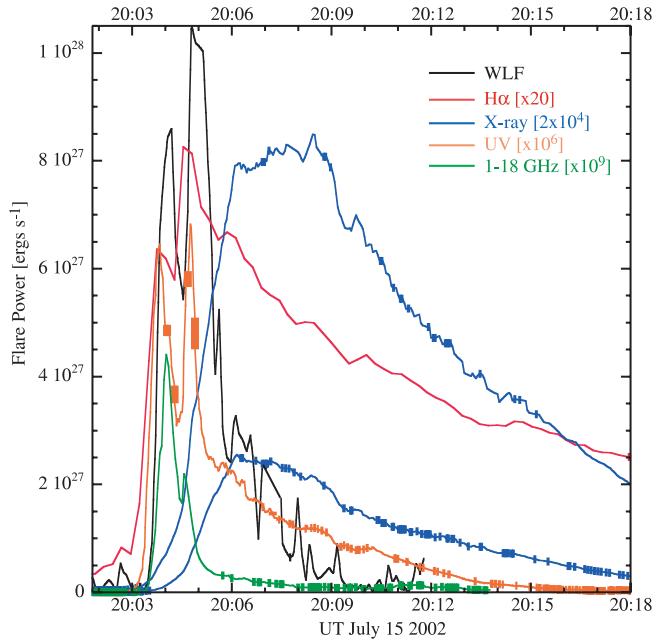


FIG. 8.—Flare emission time profiles in various wavelengths. The fluxes have been converted into power ( $\text{ergs s}^{-1}$ ) and are scaled by factors of 20 ( $\text{H}\alpha$ ),  $2 \times 10^4$  (X-ray),  $10^4$  (UV), and  $10^9$  (radio). The microwave emission is measured in solar flux units ( $1 \text{ sfu} = 10^{-22} \text{ W m}^{-2} \text{ Hz}^{-1}$ ). To obtain its power curve, we assume that the microwave emission area is equivalent to that of WLF area, and we integrated the flux over the OVSA microwave range, 1–18 GHz. To obtain X-ray power from the *GOES* data, we assume that the emission area is equivalent to that of  $\text{H}\alpha$  flare area. The C IV flare emissions were the simple sum of the intensities over the rectangular area, which is marked by a rectangle in Fig. 1, because the flare emissions dominate the brightness of images. The solar spectra are calculated by observed DN over the *TRACE* 1600 Å channel response function.

The soft X-ray began to increase at 19:48 UT. This is consistent with slow heating observed during preflare stage described in § 3.2. The impulsive phase occurred at 20:03 UT in all wavelengths, but at 20:06 UT in soft X-rays.

As seen in Figure 8, emission profiles are featured with sharp rising and slow falling properties: emissions typically peak on timescales of a dozen seconds and fall back on timescales of a dozen minutes. Because profiles are characterized with double peaks at microwave, WL,  $\text{H}\alpha$ , and UV wavelengths, the decay phases follow the second peaks. We call the period between impulsive rise and the second peak the “abrupt phase” and the period after the second peak the “gradual phase.” The microwave emission occurred only within the abrupt period, and soft X-ray emission occurred only within the gradual period.

Times of the first and the second emission peaks are slightly different depending on the wavelengths of observations. They are listed in Table 2, accurate to 1 s. The table shows that the intervals between the two emission peaks vary from 45 s (microwave) to 1 minute. In WL and  $\text{H}\alpha$ , the second peaks are higher

than the first by 20% and 30%, respectively. The sense of this asymmetry is reversed at microwave wavelengths, where the first peak is higher than the second one by about 50%. Within both peaks, WL emissions lagged  $\sim 20$  s behind the microwave peaks; this is the longest delay time among all wavelengths relative to microwave. This observation reflects that the energy sources for WLF and  $\text{H}\alpha$  probably differ from that for microwave. The Neupert effect (Dennis & Zarro 1993) was also evident, in which the soft X-ray emission lagged the first microwave burst by about 3.5 minutes. The double peaks are most naturally interpreted as two magnetic reconnection events, with the first caused by a reconnection above the “X” region and the second by a reconnection below the eruptive filament.

We estimate the WLF power at a given place and time from the WLF contrast multiplied by the solar irradiance (we assume that the optical continuum brightness enhancement due to the flare is equivalent to that detected within the IVM bandpass). The total energy released by WLF is obtained by integrating this quantity over the flare area and lifetime. In this way we find that, between 20:03 and 20:09 UT, the total energy released by the WLF is  $4.3 \times 10^{33}$  ergs. It is followed in amount by the energies released in  $\text{H}\alpha$  ( $2.4 \times 10^{31}$  ergs), X-ray ( $1.4 \times 10^{29}$  ergs), C IV ( $1.7 \times 10^{27}$  ergs), and microwave ( $2.1 \times 10^{23}$  ergs). Clearly, the WLF emission dominates the flare spectra (see Neidig 1989).

### 3.5. Flare Kernel Motion and Time Profile

Flare kernel transverse speeds, shown in Figure 4, reflect the flare emission time profiles. We give an example of WLF kernel motions and acknowledge that  $\text{H}\alpha$  and UV kernels have the same behavior. During the abrupt phase (between 20:03 and 20:05 UT), the WLF kernel moves in the plane of sky at  $263 \text{ km s}^{-1}$ . After 20:05 UT, the kernel decelerates to  $92 \text{ km s}^{-1}$ . According to conventional wisdom, flare kernels represent the footpoints of newly reconnected magnetic fields and are energized by magnetic reconnections (e.g., Fletcher & Hudson 2001). The correlation between kernel speeds and the emission time profile suggests a close relationship between the reconnection rate (for which the kernel speed is a proxy) and the energy release rate during the flare. The faster the reconnection occurs, the more radiant power is observed. Abrupt and gradual components seen in the WLF light curve remind us of the nonthermal and thermal WLF components found by Matthews et al. (2003) with *Yohkoh* observations. The speeds of kernels could well reflect the source of the flare energy, and the WLF is not fundamentally different from ordinary flares.

## 4. DISCUSSION

The time-resolved, multiwavelength observations show five important characteristics of the flare:

1. Intense heating occurred above the X region during the preflare period. This heating is then transformed into an enormous energy release signaled by abrupt emissions in all wavelengths

TABLE 2  
FLARE PEAK EMISSION TIMES (UT)

Peak	13 GHz/OVSA	1600 Å <i>TRACE</i>	$\text{H}\alpha$ /MCCD	WLF/IVM	0.5–4; 1–8 Å/ <i>GOES</i>
First .....	20:03:50	20:03:48	20:03:48	20:04:09	20:07:12; 20:08:06
Second .....	20:04:35	20:04:45	20:04:40	20:04:54	...

NOTES.—Because of seeing condition, the first WL flare peak time is uncertain by 5 s, and the second peak is uncertain by 2 s. The  $\text{H}\alpha$  emission maximum lasted from 20:04:32 to 20:04:48 UT.

and the rapid motion of the flare kernel and the ribbon straddling F1.

2. The eastern filament (F2) moved upward during the preflare phase and was dramatically accelerated when the impulsive phase set in. Less than a minute into the impulsive phase, the flare proceeded from the western neutral line to the eastern neutral line, while the filament was lifted into a loop.

3. A helix-like structure is visible in C IV/UV emission images when F2 was lifted into a loop. The helix is not cospatial with the eruptive filament, but it follows the direction of the eruptive filament.

4. A subtle, double-peaked structure is shown in the impulsive emission time profile.

5. Abrupt and gradual components of the flare emission time profile are independently reflected in the flare kernel motion transverse speeds.

To illustrate what might have happened regarding the above flare characteristics, especially the first four items, we draw a series of cartoons in Figure 9.

Figure 9a shows the preflare configuration. The active region has a quadrupolar topology. A bundle of outskirting field lines connects the leftmost and the rightmost sunspot pair, forming closed field lines in the corona. A lower bundle of field lines connecting the inner sunspot pair forms an inner arcade. As the lower magnetic loops rise, a current sheet is formed between the inner and outer magnetic flux systems (see the yellow block in the plot). The rise of loops is indicated by slow kernel/ribbon development straddling the western neutral line, H $\alpha$  red asymmetries at the site of the initial WLF, and slow upward motion of the eastern filament (F2).

Figure 9b shows the eruptive configuration. The impulsive phase begins once the balance was lost in the current sheet located high in the corona. A steady reconnection becomes a turbulent one because of the detailed physical conditions in the current sheet (e.g., Heyvaerts et al. 1977; Li et al. 1987; Chen & Shibata 2000). At this stage, the flare ribbon/kernel still straddles the western neutral line (see the first 3 rows of images in Fig. 7). The low-lying system erupted along with the filament (F2) accompanied with the first emission peak. The filament is soon lifted into a loop. A second current sheet is probably formed underneath F2 and stretched as the filament moved upward. The current sheet was stretched so thin that the reconnection took place, resulting in the displacement of the flare ribbons from the western to the eastern neutral line, and the second flare peak. Liu et al. (2003) have pointed out that at some times the C IV structure appears to have the form of a helix. It is probable that such helix is formed because of magnetic reconnection in the second current sheet (van Ballegoijen & Martens 1989). Specifically, simulations show that a converging flow toward the inversion line on the boundary will lead to the formation of a twisted flux rope by reconnection (Amari et al. 2003).

Figure 9c shows the configuration of the posteruption phase. After filament eruption, the flare emissions in UV, WL, and H $\alpha$  started to decline at 20:05 UT. The transverse motions of the flare kernels in all three wavelengths slowed down at this time (see Fig. 4). Two ribbons around the eastern neutral line were more symmetric in area and brightness than in the previous phase. They moved steadily in opposite directions over the opposite magnetic polarities, indicating the formation of postflare loops across the magnetic neutral line. Postflare loops are clearly shown in an EUV image (195 Å) taken at 20:12 UT by the Extreme Ultraviolet Imaging Telescope on board *SOHO*. Fur-

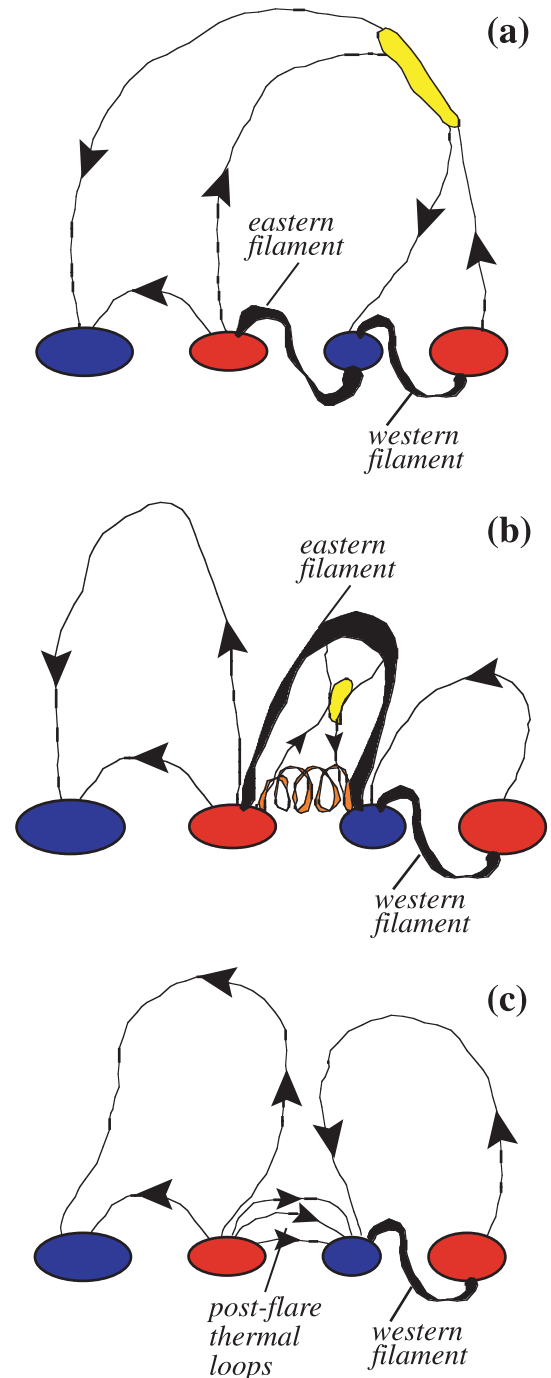


FIG. 9.—Schematic magnetic configuration above the active region during preflare and impulsive phase. The two red ellipses represent positive polarities, and the blue ones represent the negative polarities. The lines are magnetic field lines. The yellow blocks represent the reconnection sites. (a) Preflare configuration. This demonstrates the formation of a current sheet due to the rising arcade of low-lying magnetic loop. (b) Eruptive configuration. This demonstrates that a current sheet underneath the filament is stretched as the filament erupted. A helical-like structure (orange) is probably formed when the reconnections occurred within the current sheet. (c) Postflare configuration. This demonstrates the heating expansion in newly reconnected loops above the eastern neutral line.

thermore, the soft X-ray impulsive phase occurred at 20:06 UT. All these observations indicate the heating mechanism as the major source of flare energy at this postflare stage.

The photospheric converging flow discussed in § 3.1 plays a role in the current flare event. It is evident that the converging

flow of positive magnetic flux toward the eastern neutral line causes a nonpotential magnetic configuration. The convergence appears relaxed after the flare. However, it is not obvious whether the flare instability is triggered by this forceful motion. The observational evidence is that the initial flare did not occur near the fastened magnetic neutral line overlapping F2, but F1, both of which are located on the borders of opposite polarities within the quadrupolar topology. The multiarcade interaction leading to eruption has been recognized by many (e.g., Biskamp & Welter 1989). In their simulation, the rise of the inner arcade can be regarded as the result of photospheric shear motion that stretches field lines and increases the magnetic energy driving the arcade growth in both height and width. This is consistent with our observations of photospheric converging motion described in § 3.1. The result is the thermal expansion evident from the slow development of a bright kernel and ribbon straddling the western neutral line, which is demonstrated in Figure 9*a*. Therefore, the convergence could have indirectly influenced the flare in two ways: (1) it caused the local instability by generating a twisted magnetic inversion line and accumulated extra energy in the system; and (2) it provided the energy driving the magnetic loop expansion, which led to the formation of a current sheet between the rising arcade and neighboring field lines. It is the instability in the current sheet that triggers the flare.

Flares are initiated in the coronal loops have been observed in limb flares. Many of them were reported by *Yohkoh*/SXT. One example is the 1992 February 21 limb flare described by Tsuneta et al. (1992), which showed footpoint separation rate comparable to the current flare during the preflare period. The second example is mentioned in § 3.2; the X-ray observations show X-ray ejecta moving at  $\sim 10 \text{ km s}^{-1}$  during the preflare phase and accelerated to  $130 \text{ km s}^{-1}$  when the hard X-ray emission sets in (Ohyama & Shibata 1997). This is consistent with the filament Doppler shift acceleration at the moment of the impulsive rise in our work (Fig. 6). The temperature of the filament is lower than 1 MK. Its image will not show up in the soft X-ray data. The plasmoid ejection seen in the 1993 November 11 limb flare can be regarded as filament-associated material, but it is not the filament itself. As reported in the work of Ohyama & Shibata (1997), the ejecta or the filament-associated material was heated to 11.3 MK in the preflare phase, and the density was  $\sim 4.5 \times 10^9$  to  $1.4 \times 10^{10} \text{ cm}^{-3}$ . In fact, C IV images show the material erupted at 20:03:40 UT from the northern end of F2 adjacent to the filament itself erupting from the southern end. The C IV-luminous material is probably the ejecta seen in X-rays, which is the preheated material. In conclusion, the data show that the plasma temperature rose very high above the filament before the impulsive phase, consistent with the preheating straddling F2 and intense heating observed at the initial WLF site.

## 5. SUMMARY

We describe time-resolved, multiwavelength observations of an X3 flare that occurred on 2002 July 15 between 20:03 and 20:09 UT within NOAA AR 10030 (N18°, E00°). Notable features include a white-light flare, a filament eruption seen in the chromosphere, and a helical structure eruption seen in the transition region. Observations were made with a collective data set, which allows us to compare flare powers in various wavelength bands and to examine the filament eruption process. We summarize the observations as follows:

1. NOAA AR 10030 has a quadrupolar topology, where the flare occurs. Strong photospheric converging flow toward the

magnetic neutral line results in the expansion of inner loops, which then interact with outer loops. Magnetic reconnections occur in high corona, possibly in a current sheet formed between inner and outer loop systems. Then the low-lying magnetic system is released to eruption.

2. Observational evidence on preflare heating is consistent with limb flare observations made by *Yohkoh*/SXT. Magnetic loop thermal expansion during the preflare period results in the bright ribbon/kernel slow separation straddling the magnetic neutral line.

3. A filament moves upward during preflare period; it is greatly accelerated at the impulsive rise.

4. Double impulsive emission peaks were observed at nearly all wavelengths from UV to radio, probably caused by two distinct magnetic reconnection events. The first impulsive peak is caused by high-altitude reconnection. The second impulsive peak is associated with a filament eruption that triggers a second reconnection underneath the filament.

5. A three-twist helical flux rope erupts 1 minute later than the filament. Observations do not exclude the hypothesis that the photospheric convergence could be responsible for the formation of such structure by reconnections. Its eruption is consistent in time with the entire filament being lifted into a loop by the eruption.

6. The maximum flare powers ( $\text{ergs s}^{-1}$ ) are  $10^{28}$  in WLF,  $4 \times 10^{26}$  in H $\alpha$ ,  $4.2 \times 10^{23}$  in soft X-ray,  $6.4 \times 10^{21}$  in C IV/UV, and  $4.3 \times 10^{18}$  in 1–18 GHz radio. WLF emission dominates the flare spectra.

7. During the flare impulsive phase, the time profile shows both abrupt and gradual components. The microwave occurs only during the abrupt phase, and soft X-ray impulsive onset occurs only during the gradual phase. Major features of flare power profile are independently reflected in the speeds of flare kernels.

8. The WLF is not fundamentally different from flares at other wavelengths. It behaves in the same way as flares in other wavelengths, except that the WLF peaks are lagged behind the microwave burst by the longest time, and it has the shortest lifetime (among H $\alpha$ , UV, and WL emissions).

During the process of this work, J. L. has discussed the event with many research fellows at meetings SPD 2003 (APL) and SHINE 2003 (Maui). We are thankful to all of the colleagues who have discussed this flare with us. We especially thank the referee, who provided valuable comments that inspired the authors to focus on the most important observations and to draw clear conclusions. J. L. thanks Dave Jewitt for reading the entire draft and improving the text in numerous places. J. L. is supported by NASA grant NAG 12880, the MURI program SA 3208 (Air Force F49620-01-1-0360), and a subcontract of the NASA grant “Velocity Structure and Plasma Properties of Halo CMEs,” awarded to the Smithsonian Astrophysical Observatory and the University of Hawaii (SV3-73017). B. J. L. is supported by NASA grants NAG 513021 and NAG 13505. *SOHO* is a project of international cooperation between the ESA and NASA. *TRACE* is a mission of the Stanford-Lockheed Institute for Space Research and part of the NASA Small Explorer program. The Big Bear Solar Observatory and Owens Valley Solar Array are maintained and operated by the Center for Solar Research at the New Jersey Institute of Technology.

## REFERENCES

- Abbett, W. P., & Hawley, S. L. 1999, *ApJ*, 521, 906  
Amari, T., Luciani, J. F., & Aly, J. J. 2003, *ApJ*, 585, 1073  
Antiochos, S. K. 1998, *ApJ*, 502, L181  
Antiochos, S. K., DeVore, C. R., & Klimchuk, J. A. 1999, *ApJ*, 510, 485  
Biskamp, D., & Welter, H. 1989, *Sol. Phys.*, 120, 49  
Brown, D. S., Nightingale, R. W., Alexander, D., Schrijver, C. J., Metcalf, T. R., Shine, R. A., Title, A. M., & Wolfson, C. J. 2003, *Sol. Phys.*, 216, 79  
Chen, P. F., & Shibata, K. 2000, *ApJ*, 545, 524  
Dennis, B. R., & Zarro, D. M. 1993, *Sol. Phys.*, 146, 177  
Fletcher, L., & Hudson, H. 2001, *Sol. Phys.*, 204, 69  
Freeland, S. L., & Handy, B. N. 1998, *Sol. Phys.*, 182, 497  
Gary, A., & Moore, R. L. 2004, *ApJ*, 611, 545  
Handy, B. N. 1999, *Sol. Phys.*, 187, 229  
Heyvaerts, J., Priest, E. R., & Rust, D. M. 1977, *ApJ*, 216, 123  
Hudson, H. S. 1972, *Sol. Phys.*, 24, 414  
Ichimoto, K., & Kurokawa, H. 1984, *Sol. Phys.*, 93, 105  
Kahler, S. W., Moore, R. L., Kane, S. R., & Zirin, H. 1988, *ApJ*, 328, 824  
Li, H.-W., Pallavicini, R., & Cheng, C.-C. 1987, *Sol. Phys.*, 107, 271  
Liu, Y., Jiang, Y. C., Ji, H. S., Zhang, H. Q., & Wang, H. M. 2003, *ApJ*, 593, L137  
Matthews, S. A., van Driel-Gesztelyi, L., Hudson, H. S., & Nitta, N. V. 2003, *A&A*, 409, 1107  
McIntosh, P. S., & Donnelly, R. F. 1972, *Sol. Phys.*, 23, 444  
Metcalf, T. R., Alexander, D., Hudson, H. S., & Longcope, D. W. 2003, *ApJ*, 595, 483  
Mickey, D. L., Canfield, R. C., LaBonte, B. J., Leka, K. D., Waterson, M. F., & Weber, H. M. 1996, *Sol. Phys.*, 168, 229  
Neidig, D. F. 1989, *Sol. Phys.*, 121, 261  
Neidig, D. F., Kiplinger, A. L., Cohl, H. S., & Wiborg, P. H. 1993, *ApJ*, 406, 306  
Neidig, F. N., & Cliver, E. W. 1983, *Sol. Phys.*, 88, 275  
Ohyama, M., & Shibata, K. 1997, *PASJ*, 49, 249  
Penn, M. J., Mickey, D. L., Canfield, R. C., & LaBonte, B. J. 1991, *Sol. Phys.*, 135, 163  
Sylwester, B., & Sylwester, J. 2000, *Sol. Phys.*, 194, 305  
Tang, F. 1983, *Sol. Phys.*, 83, 15  
Tsuneta, S., Hara, H., Shimizu, T., Acton, L. W., Strong, K. T., Hudson, H. S., & Ogawara, Y. 1992, *PASJ*, 44, L63  
van Ballegoijen, A. A., & Martens, P. C. 1989, *ApJ*, 343, 971